Available online at www.sciencedirect.com
ScienceDirect
Journal of the European Ceramic Society 28 (2008) 91–99
www.elsevier.com/locate/jeurceramsoc

Phase transformations and microstructures of TiO_2–SnO_2 due to solution annealing versus reactive sintering

Hui-Chiao Yu, Pouyan Shen *

Institute of Materials Science and Engineering, National Sun Yat-sen University, Kaohsiung 804, Taiwan, ROC

Received 21 March 2007; accepted 2 June 2007
Available online 23 August 2007

Abstract

TiO_2–SnO_2 in molar ratios of 2:8, 5:5 and 8:2 were subject to solution annealing, or alternatively prepared by a reactive sintering route, for X-ray diffraction and analytical electron microscopic studies. Defect clusters and commensurate superstructures were formed in the TiO_2–SnO_2 solid solution of the rutile-type structure when quenched from 1600 °C in air. Upon annealing and decomposition outside the spinodal at 1000 °C, a metastable ilmenite-type phase was precipitated from the rutile structure. This is in drastic contrast to the spinodal decomposition along [0 0 1] to form a semi-coherent (0 0 1) interface. An alternative phase-equilibrium route by reactive sintering at 1000 °C was facilitated by rapid interdiffusion and Brownian rotation of smaller-sized SnO_2 particles until parallel epitaxial relationship with the TiO_2-rich host was reached.

Keywords: Phase transformation; Brownian motion; TiO_2–SnO_2; Annealing; Reactive sintering; Electron microscopy

1. Introduction

A complete solid solution between TiO_2 (rutile, denoted as r) and SnO_2 (cassiterite) with the space group $P4_2/mnm$ at high-temperatures is very well documented. This binary system has a nearly symmetric miscibility gap for spontaneous spinodal decomposition,[1–5] with the critical composition 47 ± 2 mol% TiO_2 at 1430 ± 5 °C according to the updated phase diagram.[4] The experimental results[2,3] showed that the decomposition of equimolar TiO_2–SnO_2 alloy produces composition fluctuation along [0 0 1], and theoretical calculation indicated the spinodal is 105 °C below the solvus.[4] The combined experimental results of X-ray diffraction (XRD) and electron diffraction[5] further indicated that the alloys within the spinodal can decompose by a continuous and spontaneous process; whereas alloys outside the spinodal by a nucleation and growth process.

Despite the large amount of previous data available on this system, especially in the region of spontaneous spinodal decomposition, it is not known whether Guinier–Preston (G.P.) zones and/or other metastable phases occur for TiO_2–SnO_2 binary upon exsolution, and whether the Sn^{4+} substitution for Ti^{4+} could cause defect clusters and/or commensurate superstructures analogous to Ti^{4+}-dissolved MgO,[6] and Zr^{4+}-doped TiO_2,[7] at a certain extent of undercooling with respect to the phase boundaries. (Upon cooling and exsolution, the Ti^{4+}-dissolved MgO forms G.P. zones and then nanometer-size Mg_2TiO_4 spinel with {1 1 1} and {0 0 1} facets,[6] whereas the Zr-doped TiO_2 forms plate-like G.P. zone with the plate surface parallel to (1 0 0) and (0 1 0) in association with dislocations.[7] Diffuse diffractions as a result of Zr^{4+} substitution for Ti^{4+} with volume/charge compensating defect clusters and commensurate superstructures with apparent triple {1 0 1} and {1 1 1} periodicity also occurred as metastable intermediates, which are presumably the precursor of the equilibrium $ZrTi_2O_6$ precipitate.[7])

The motivation of this research is to study non-equilibrium phase transformations and phase behavior of TiO_2–SnO_2 binary, and to compare results from the two different synthesis routes of solution annealing versus reactive sintering. By an alternative reactive sintering route, we aim to prove that short-circuit interdiffusion between the necking TiO_2 and SnO_2 powders facilitates the phase equilibrium, as well as the Brownian type rotation of the small-sized particles to reach low-energy epitaxial state with respect to the host grains. The later process is analogous to thermally activated and oxidation-decomposition facilitated Brownian rotation of crystallites in the $(Ni_mCo_{1-m})_{1-\delta}O$ polycrystals.[8] (Refer to Appendix A for

* Corresponding author.
E-mail address: pshen@mail.nsysu.edu.tw (P. Shen).

0955-2219/$ – see front matter © 2007 Elsevier Ltd. All rights reserved.
doi:10.1016/j.jeurceramsoc.2007.06.016

thermally activated Brownian rotation of crystallites over a crystalline substrate or within a host grain typically prepared via a solid state sintering route.[9–22])

2. Experimental

TiO_2 (Aldrich, 99.9%, 4 μm in particle size) and SnO_2 powders (Acros, 99.9%, 1 μm in particle size) in mole ratios 2:8, 5:5 and 8:2 (denoted as 2T8S, 5T5S and 8T2S, respectively) were dry-pressed at 650 MPa into disks 10 mm in diameter and 2 mm in thickness. The pellets were then homogenized at 1600 °C for 4 h followed by air quenching to room temperature with or without further annealing at 1000 °C for 12 h or 72 h followed by cooling in air. Alternatively, the dry-pressed pellets were reactively sintered at 1000 °C for 72 h followed by air-quenching to room temperature.

The fired specimens were analyzed by XRD (Cu Kα, 40 kV, 30 mA, using Siemens D5000 diffractometer) in the 2θ range of 20–70° at a scanning rate of 1°/min (step size 0.05°, fixed counts 3 s) to identify the crystalline phases. The d-spacing measured from XRD traces were used for least-squares refinement of the lattice parameters.

The fired specimens more or less sintered were polished for scanning electron microscopic (SEM, JEOL JSM-6400, 20 kV) observations. Secondary electron image (SEI) and backscattered electron image (BEI) were used to characterize the grain size and the composition distribution.

Thin sections of the fired samples were also Ar-ion milled to electron transparency for analytical electron microscopic (AEM, JEOL3010, 300 kV) observations coupled with energy dispersive X-ray (EDX) analysis. Bright field image (BFI) and dark field image (DFI) taken by transmission electron microscopy (TEM) were used to study the microstructures. Selected area electron diffraction (SAED) pattern and lattice image coupled with two-dimensional Fourier transform and inverse transform were used to characterize defect clusters and metastable phases, if any.

3. Results

3.1. XRD

3.1.1. Samples quenched from 1600 °C

XRD traces (not shown) indicated that the 2T8S, 5T5S and 8T2S samples homogenized at 1600 °C for 4 h and then quenched to room temperature in air have a single phase of solid solution between TiO_2 and SnO_2, in accordance with the phase diagram.[4] According to least-squares refinement of the d-spacings measured from the XRD trace, the rutile solid solution of the representative 5T5S sample has lattice parameters $\boldsymbol{a} = 0.4663 \pm 0.0002$ nm, $\boldsymbol{c} = 0.3060 \pm 0.0002$ nm, which are larger than those of the undoped TiO_2 rutile ($\boldsymbol{a} = 0.4593$ nm, $\boldsymbol{c} = 0.2959$ nm, JCPDS file 21-1276). The increased lattice parameter of the Sn-dissolved rutile is consistent with the substitution of larger-size Sn^{4+} (0.069 nm) for Ti^{4+} (0.061 nm), both radii are effective in coordination number (CN) of 6.[23]

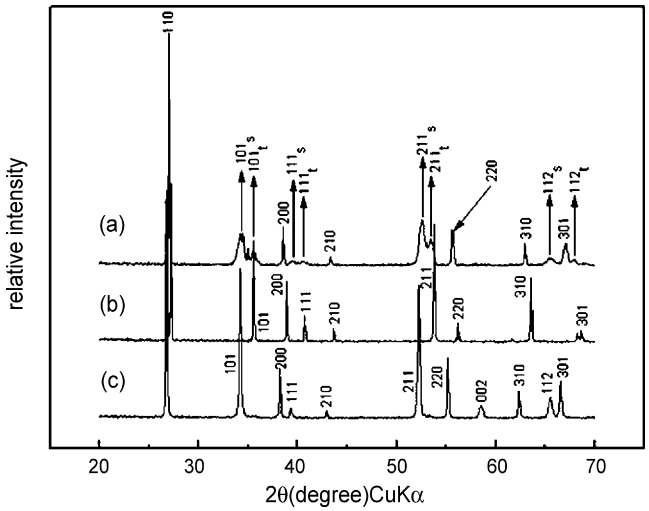

Fig. 1. XRD traces of (a) 5T5S, (b) 8T2S and (c) 2T8S samples having been sintered/homogenized at 1600 °C for 4 h and then annealed at 1000 °C for 72 h followed by air-quenching to room temperature, showing significant phase separation as TiO_2-rich and SnO_2-rich rutile phase (denoted as t and s, respectively) for the 5T5S specimen. Note the side bands due to phase separation are distinct for (1 0 1), (1 1 1), (2 1 1) and (1 1 2), but not the planes in the [0 0 1] zone axis (cf. text).

3.1.2. Samples solution annealed at 1000 °C

XRD traces of the 2T8S, 5T5S and 8T2S samples homogenized at 1600 °C and then annealed at 1000 °C for 72 h indicated that only the 5T5S specimen shows side bands as a result of spinodal decomposition (Fig. 1). The side bands are distinct for (1 0 1), (1 1 1), (2 1 1) and (1 1 2), but not the planes in the [0 0 1] zone axis (i.e. (1 1 0), (2 0 0), (2 1 0), (2 2 0) and (3 0 1)), in accord with previous observations of side bands for *hkl* reflections with $l \neq 0$ by XRD.[2,3] There is a lower diffraction intensity of the (1 0 1), (1 1 1), (2 1 1) and (1 1 2) due to preferred decomposition of such planes. The absence of (0 0 2) diffraction peak for the 5T5S and 8T2S but not 2T8S specimen can be attributed to preferred orientation of the coarsened grains as indicated by SEM observations of the grains as large as 10–20 μm for the homogenized and then annealed specimens (cf. Appendix Ba).

3.1.3. Samples reactively sintered at 1000 °C

For the samples reactively sintered at 1000 °C for 72 h, there are two rutile phases with distinct lattice parameters regardless of the bulk composition (Fig. 2), e.g. $\boldsymbol{a} = 0.4610$ nm, $\boldsymbol{c} = 0.2980$ nm and $\boldsymbol{a} = 0.4734$ nm, $\boldsymbol{c} = 0.3184$ nm for Ti-rich and Sn-rich composition, respectively for the 5T5S specimen (Table 1). The two phases have the near equilibrium compositions 9T1S and 1T9S, respectively assuming linear composition dependence of lattice parameters given $\boldsymbol{a} = 0.4593$ nm, $\boldsymbol{c} = 0.2959$ nm for TiO_2 rutile (JCPDS file 21-1276) and $\boldsymbol{a} = 0.4738$ nm, $\boldsymbol{c} = 0.3187$ nm for the rutile-type SnO_2 (JCPDS file 21-125). The diffraction intensity depends more on the relative proportion of the two phases than the preferred orientation of the coarsened grains because the grain size hardly exceeds 5 μm in these specimens (cf. Appendix Bb).

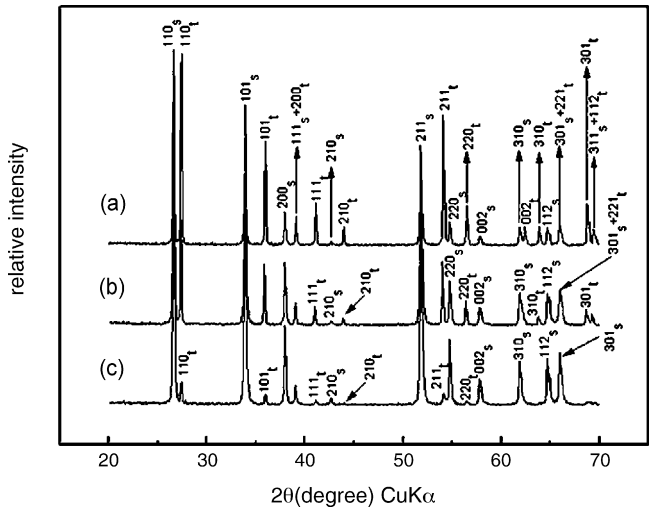

Fig. 2. XRD traces of (a) 8T2S, (b) 5T5S and (c) 2T8S samples reactively sintered at 1000 °C for 72 h followed by air-quenching to room temperature, showing significant phase separation as TiO_2-rich and SnO_2-rich rutile phase (denoted as t and s, respectively) for all the specimens.

3.2. TEM

3.2.1. Samples quenched from 1600 °C

The 2T8S sample homogenized at 1600 °C followed by air-quenching to room temperature shows tweed contrast in BFI (Fig. 3a) and superlattice spots at 1/3 and 2/3(3 2 1) in corresponding SAED pattern (Fig. 3b) of the SnO_2-rich rutile phase. The 5T5S sample, homogenized and cooled under the same conditions also shows tweed contrast (Fig. 4a) and diffuse diffraction intensity near 1/2G(0 1 1) reciprocal space of the rutile phase (Fig. 4b). Lattice image (Fig. 5a) and reconstructed image of the rutile phase in this specimen (Fig. 5b) further reveal dislocations with half plane parallel to (1 0 0) presumably due to the size mismatch of Ti^{4+} and Sn^{4+} in substitution.

3.2.2. Samples solution annealed at 1000 °C

The 2T8S solid solution annealed at 1000 °C (i.e. outside the [0 0 1] coherent spinodal[4,5]) for 72 h shows plate-like Bragg

Table 1
Molar compositions and lattice parameters of dual rutile phases in 2T8S, 5T5S and 8T2S samples prepared by reactive sintering at 1000 °C for 72 h

Sample and phase compositions		
	a (nm)	***c*** (nm)
2T8S		
1T9S	0.4734 ± 0.0001	0.3185 ± 0.0001
9T1S	0.4603 ± 0.0001	0.2972 ± 0.0001
5T5S		
1T9S	0.4734 ± 0.0001	0.3184 ± 0.0001
9T1S	0.4.610 ± 0.0001	0.2980 ± 0.0001
8T2S		
1T9S	0.4736 ± 0.0006	0.3179 ± 0.0007
9T1S	0.4.607 ± 0.0005	0.2982 ± 0.0006

The lattice parameters are based on least-squares refinement of the d-spacings measured from XRD traces in Fig. 2.

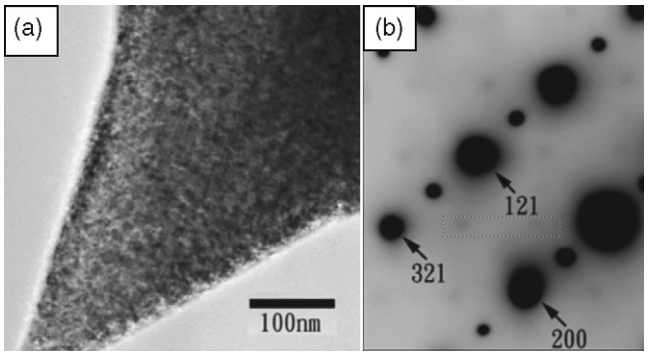

Fig. 3. TEM (a) BFI and (b) SAED pattern of 2T8S sample sintered/homogenized at 1600 °C for 4 h followed by air-quenching to room temperature, showing tweed contrast and superlattice spots 1/3 and 2/3(3 2 1) (as encompassed by dotted line) of SnO_2-rich rutile phase.

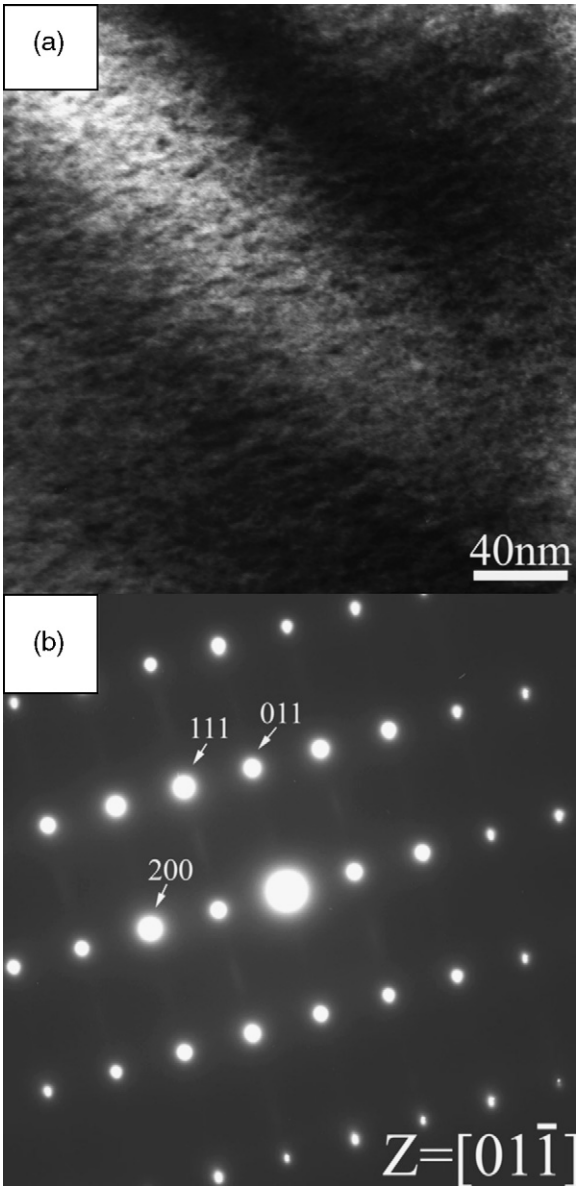

Fig. 4. TEM (a) BFI and (b) SAED pattern ($Z = [0\,1\,\bar{1}]$) of 5T5S sample sintered/homogenized at 1600 °C for 4 h followed by air-quenching to room temperature, showing tweed contrast and diffuse diffraction intensity near 1/2G(0 1 1) reciprocal space of the rutile phase.

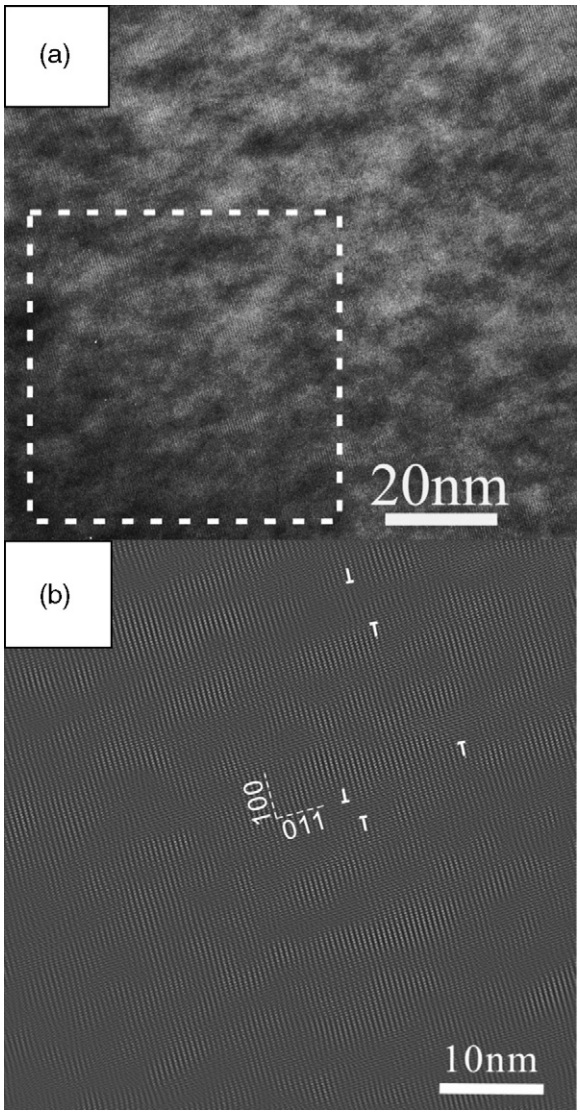

Fig. 5. TEM (a) lattice image and (b) reconstructed image of the square region of the rutile phase in (a) showing dislocations (denoted by T) with half plane parallel to (1 0 0) in 5T5S sample quenched from 1600 °C. It is the same specimen as in Fig. 4.

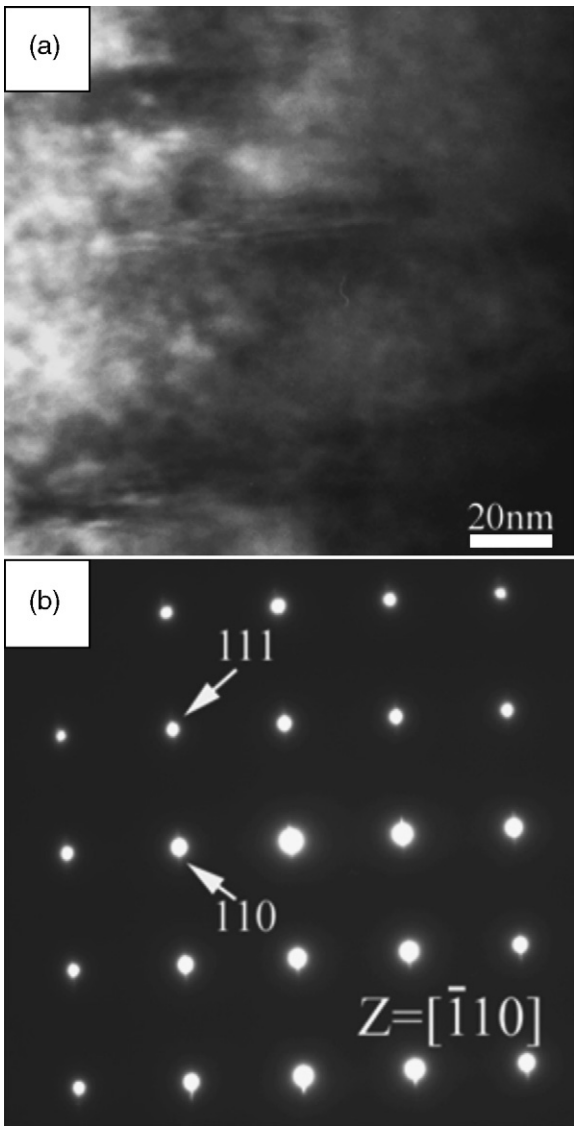

Fig. 6. TEM (a) BFI and (b) SAED pattern ($Z = [\bar{1}\,1\,0]$) of 2T8S sample sintered/homogenized at 1600 °C for 4 h and then annealed at 1000 °C for 72 h followed by air-quenching to room temperature, showing side band diffractions along [0 0 1] reciprocal direction of the rutile phase.

contrast parallel to (0 0 1) (Fig. 6a) and side band diffractions along [0 0 1] direction as shown by the SAED pattern in $[\bar{1}\,1\,0]$ zone axis (Fig. 6b). These features became vague when the sample was tilted to $[0\,\bar{1}\,0]$ zone axis (Fig. 7). Such plate-like Bragg contrast and side band diffractions are presumably due to early decomposition in view of the similar features observed for the equimolar alloy after initial-stage decomposition at 900 °C (cf. Fig. 6 of ref.[5] Lattice image (Fig. 8a) and 2 D Fourier transform and inverse transform (Fig. 8b and c, respectively) further resolve minor ilmenite (denoted as i) -type phase in epitaxial association with the rutile host in this zone axis. The $2/3(\bar{1}\,0\,1)$ superlattice spots of the rutile structure, appeared to be hematite-type analogous to Fe-bearing hematite-type precipitates in metamorphic rutile.[24] However, the presence of (1 0 0) superlattice diffraction of rutile (Fig. 8b) indicates that there is further ordering along the crystallographic ***c***-axis of the hematite type precipitate into ilmenite-type structure (space group $R\bar{3}$, #148) with allowed (0 0 0 3) reflection, i.e. the forbidden position of $1/2(2\,0\,0)_r$, which should otherwise be absent for rutile- (space group $P4_2/mnm$, #136) and hematite-type (space group $R\bar{3}c$, #167) structure. The SAED pattern in Fig. 8b can be interpreted as the single ilmenite-type variant superimposed with the rutile following the crystallographic relationship $(0\,0\,1)_i//(1\,0\,0)_r$; $[1\,0\,0]_i//[0\,1\,0]_r$ analogous to that indexed in Fig. 12c of ref.[24] for the epitaxial hematite-type precipitates in metamorphic rutile. It is difficult, if not impossible, to do EDX or electron energy loss spectroscopic analysis of the chemical composition of the nano-size ilmenite-type precipitate in the rutile-type host. Still, the ilmenite-type precipitate is expected to contain ordered Ti^{4+} and Sn^{2+} upon solution annealing at 1000 °C as discussed later. There is an additional epitaxial phase as indicated by the allowed diffractions (i.e. not double diffractions) circled

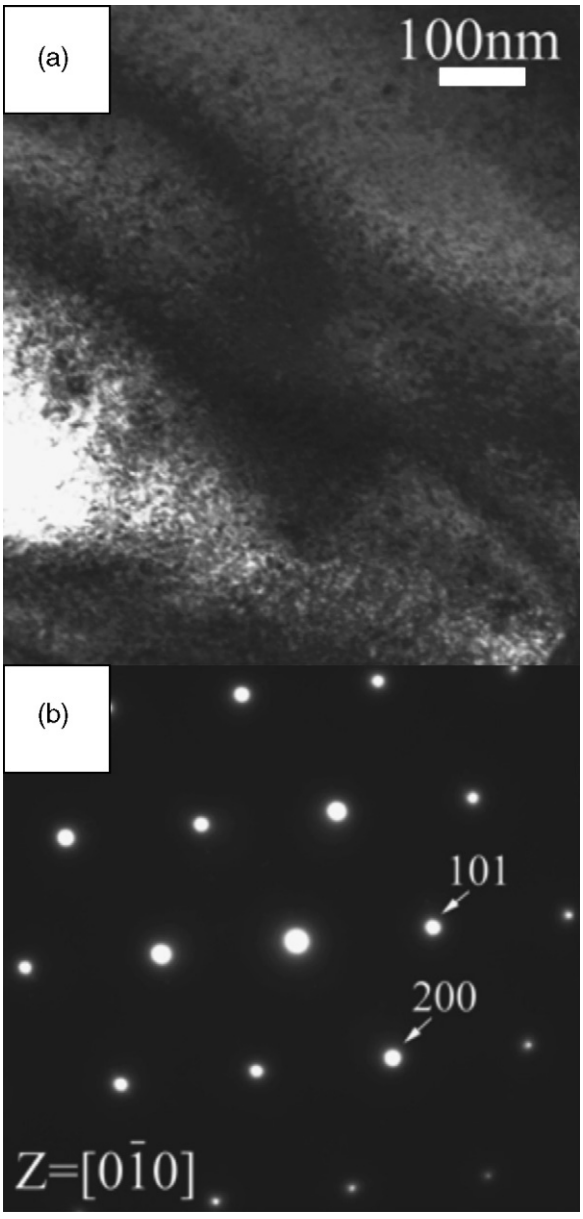

Fig. 7. TEM (a) BFI and (b) SAED pattern of the rutile phase in the same specimen solution annealed as in Fig. 6 but tilted to [0 $\bar{1}$ 0] zone axis showing negligible side band diffractions.

in Fig. 8b, and the inverse transform of such spots in Fig. 8c. This metastable phase shares the (1 0 1) reflection of the rutile and could be attributed to a nonstoichiometric phase analogous to undoped nonstoichiometric titania[25,26] as discussed later.

The equimolar alloy with a much larger extent of oversaturation than the un-equalmolar alloys underwent significant spinodal decomposition upon annealing at 1000 °C for only 12 h. The composition fluctuation with a periodicity of ca. 15 nm occurred predominantly along [0 0 1] direction as indicated by lattice image and inset SAED pattern in [$\bar{1}$ 1 0] zone axis (Fig. 9a). The reconstructed image further revealed misfit dislocations with half plane parallel to (1 1 0) along the semi-coherent (0 0 1) interface (Fig. 9b).

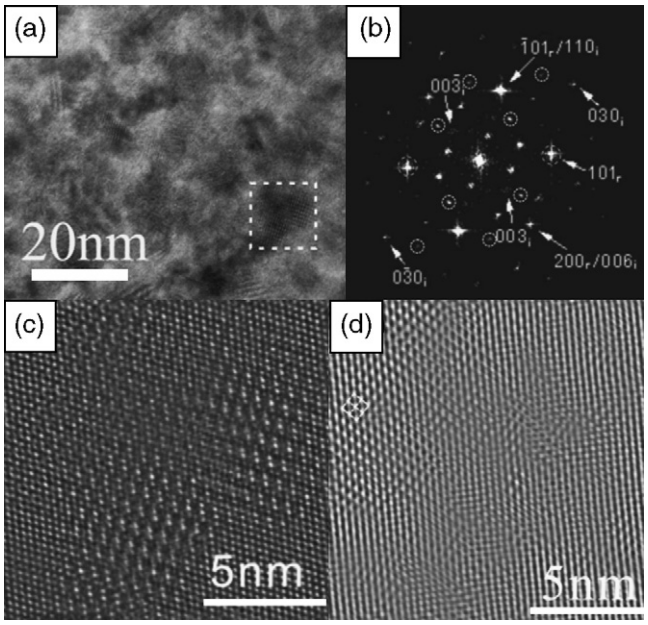

Fig. 8. TEM (a) lattice image, (b) and (c) 2 D Fourier transform and inverse transform, respectively from the square region in (a) showing ilmenite-type phase in epitaxial association with the rutile host in [0 $\bar{1}$ 0] zone axis as the case in Fig. 7. (d) Additional lattice (as denoted by white lines) revealed by inverse transform of the extra diffractions circled in (b), which is tentatively attributed to a nonstoichiometric phase analogous to undoped nonstoichiometric titania (cf. text). It is the same specimen annealed at 1000 °C as in Figs. 6 and 7.

3.2.3. Samples reactively sintered at 1000 °C

The BFI and DFI with inset SAED pattern for the sample reactively sintered at 1000 °C for 72 h (Fig. 10) show that the smaller and relatively SnO_2-rich particles tended to be encompassed and became parallel epitaxial with respect to the TiO_2-rich host having dislocations at the relic interface. This is due to Brownian motion of the small particles as discussed in Section 4.4.

4. Discussion

4.1. Defects due to SnO_2–TiO_2 solid solution

Diffuse diffractions, superlattice spots and dislocations were found for the present samples fired at temperatures in air. The specific types of these defects are beyond the scope of the present study. Still, the genesis of such defects can be explained by the following defect chemistry consideration.

TiO_2 is in fact nonstoichiometric TiO_{2-x} with relatively high diffusion rate due to high concentration of defects such as double ionized oxygen vacancies and Ti^{4+} or Ti^{3+} interstitials.[27] On the other hand, SnO_2 has a strong character of both covalent and ionic bonding and hence slower diffusion rate involving free surface diffusion at low temperature (500–1000 °C) whereas evaporation–condensation at high-temperature ($T > 1300$ °C).[28]

The SnO_2 and TiO_2 solid solution in the rutile structure involves not only substitution of isovalent cations Ti^{4+} and Sn^{4+}, but also charge compensating defects when a cation is in an

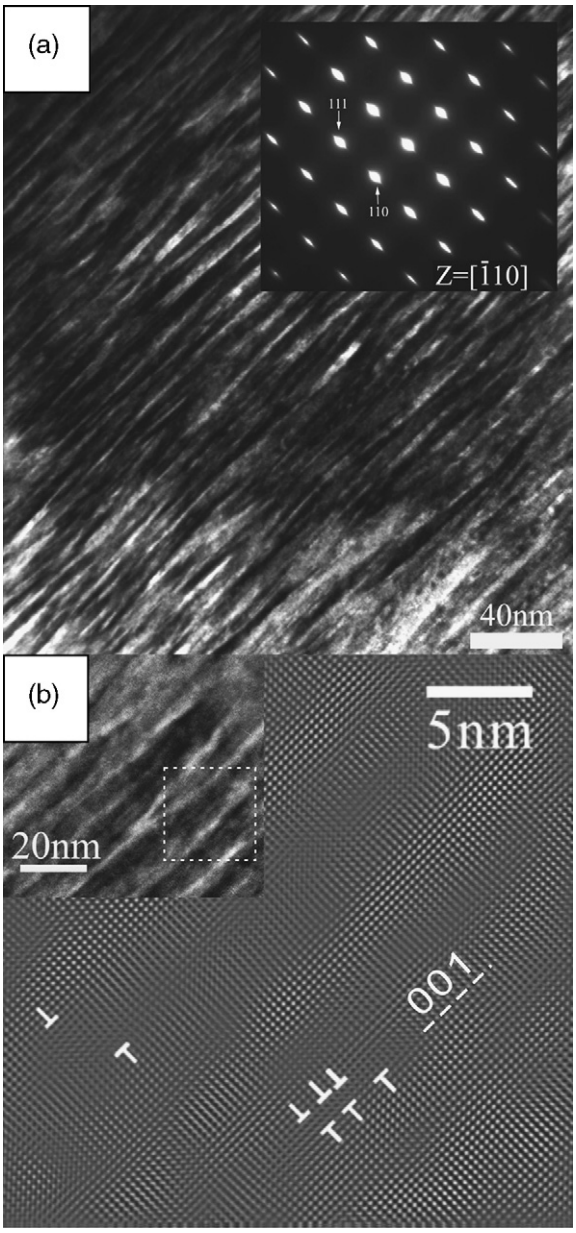

Fig. 9. TEM (a) lattice image and inset SAED pattern ($Z = [\bar{1}10]$) of 5T5S sample sintered/homogenized at 1600 °C for 4 h and then annealed at 1000 °C for 12 h followed by air-quenching to room temperature, showing significant spinodal decomposition along [0 0 1] direction and (b) reconstructed image from the square region in the inset lattice image showing misfit dislocations with half plane parallel to (1 1 0) along the semi-coherent (0 0 1) interface.

interstitial site leaving a cation vacancy or when Sn^{4+} reduces at high-temperatures leading to oxygen vacancies.[29] (The main diffusion mechanism of TiO_2–SnO_2 system is governed by the diffusion of interstitial titanium atom and Ti vacancies at 1000 °C.[29] Oxygen vacancies could also be present as intrinsic defects at high-temperature in accompaniment with the reduction of Sn^{4+} to Sn^{2+} to maintain electron neutrality.[29]) The ordering of Ti^{4+} and Sn^{2+} in substitution of Ti^{4+} (i.e. Sn_{Ti} in Kröger-Vink notation[30]) with charge compensating defects may account for the metastable precipitation of ilmenite-type structure at 1000 °C. The substitution of larger-size cations would also cause volume-compensating ion vacancies. A large internal stress due to cation size mismatch at 1000 °C, a moderate homologous temperature (i.e. T/T_m, where T_m is melting point in Kelvin) of 0.60–0.67 given T_m = 2113 K and 1898 K for rutile-type TiO_2 and SnO_2, respectively, could then cause plastic deformation of the crystal, as manifested by the presence of dislocations in Fig. 5b.

Fig. 10. TEM (a) BFI and (b) DFI (g = 200) with inset SAED pattern of 2T8S sample reactively sintered at 1000 °C for 72 h followed by air-quenching to room temperature, showing the smaller and relatively SnO_2-rich particles (e.g. the one pointed out by an arrow in (a)) were encompassed and became parallel epitaxial with respect to the TiO_2-rich host due to Brownian motion of the small particles (cf. text).

4.2. Spontaneous spinodal decomposition via anisotropic lattice diffusion

The equimolar alloy in 5T5S specimen showed significant spinodal decomposition upon annealing at 1000 °C. According to theoretical considerations of Khachaturyan,[31] the evolution of two coexisting cubic solid solutions with incoherent interfaces from a single-phase cubic solid solution occurs in three

stages forming, respectively, coherent compositional modulations, alternate lamellae of differing compositions coherently fitted along interfaces orthogonal to the direction of the modulation, and then incoherent interfaces where the strain mismatch is accommodated by interface dislocations. The decomposition of TiO_2–SnO_2 solid solution within the spinodal was also known to involve coherency loss. The composition fluctuation is however quite anisotropic, i.e. preferred to occur along [0 0 1] as mentioned,[2–4] and causes dislocations according to the decomposition kinetic studies with aliovalent dopants.[32] (The kinetics of decomposition was strongly influenced by the type and the amount of dopant. Specifically, Al^{3+} enhanced the decomposition while Ta^{+5} suppressed it, presumably due to a greater cation interstitial mobility than cation vacancy mobility.[32]) In fact, the side bands for *hkl* reflections with $l \neq 0$, as mentioned, can be attributed to the anisotropy in elastic free energy[2,3] as well as the anisotropies in the diffusion mobility and in the gradient energy.[33]

Regarding diffusion anisotropy, it is of interest to note that the rutile lattice has "channels" of low electron density along rutile ***c***-axis, which lead to greatly enhanced interstitial diffusion of Ni^{2+}, compared to diffusion via substitutional lattice sites.[34,35] Note also the misfit dislocations as a result of coherency loss at the (0 0 1) interface appeared to have (0 0 1) slip plane (Fig. 9b). By contrast, the slip plane, or fault/twinning plane is (0 1 1), i.e. the closest packing plane of the rutile structure, for (0 1 1)-specific coalesced condensates of the rutile-type TiO_2,[36] and SnO_2.[37] It is possible that anisotropic interdiffusion and hence predominant composition fluctuation along the ***c***-axis caused unusual (0 0 1) slip plane for the rutile type structure upon spontaneous spinodal decomposition.

4.3. Metastable phase selection upon nonspontaneous decomposition

The non-equimolar alloy in 8T2S specimen showed ilmenite-type precipitate and another epitaxial phase in the rutile structure host upon nonspontaneous decomposition at 1000 °C. These metastable precipitates apparently have favorable lower energy barrier of nucleation analogous to the formation of G.P. zones and commensurate superstructures in Ti^{4+}-dissolved MgO,[6] and Zr^{4+}-doped TiO_2.[7] The rate of interdiffusion between TiO_2 and SnO_2 is of concern to the common tangent, i.e. chemical potential, of the chemical free energy curves of the metastable precipitates phase and the rutile phase at a given undercooling with respect to the solvus. The structure similarity, and hence interfacial/strain energetics, as well as defect species and ordering are also important on the metastable phase selection for the nonspontaneous decomposed TiO_2–SnO_2 alloy.

The exsolution of metastable plate-like ilmenite-type and commensurate superstructures from Ti-dissolved rutile-type SnO_2 may take advantage of the relatively weak linkage of the planes in the [0 0 1] zone axis due to the volume compensating oxygen vacancies. The allowed $2/3(\bar{1}\,0\,1)$ diffraction and apparent tripling of the $(\bar{1}\,0\,1)$ spacing due to dynamic diffraction as well as the doubling of (1 0 0) spacing of the rutile type structure can be attributed to an ordered hematite-type, i.e. ilmenite-type structure. In this connection, the Fe-bearing twin platelets in metamorphic rutile have been identified to be of the corundum isostructure of hematite (or Ti_2O_3).[24] (These twin platelets are coherently intergrown parallel to (1 0 0) and (0 1 0) of metamorphic rutile and the dynamic diffraction effect induces the apparent tripling of the {1 0 1} spacings.[24]) In fact, the epitaxial precipitation of ilmenite with $(0\,0\,1)_i//(1\,0\,0)_r$; $[1\,0\,0]_i//[0\,1\,0]_r$ is analogous to the epitaxial precipitation of hematite type variants in metamorphic rutile following $(0\,0\,1)_h//(1\,0\,0)_r$; $\langle 1\,0\,0\rangle_h//[0\,1\,0]_r$,[24] except there is long range ordering along the ***c***-axis for the ilmenite- not the hematite-type structure. The fair lattice match for $(0\,0\,6)_i/(2\,0\,0)_r$ and $(1\,1\,0)_i/(\bar{1}\,0\,1)_r$ planes (Fig. 8b) may account for a low interfacial energy and strain energy for the metastable precipitation selection of the ilmenite-type phase. It is noteworthy that the Sn^{4+}/Sn^{2+} and Ti^{4+} ordering to form commensurate superstructure might proceed simultaneously with defect clustering in the Ti-dissolved rutile type SnO_2 upon solution annealing at 1000 °C. In this connection, recent theoretical calculations, considering the interactions with the second nearest neighbors in addition to the first ones, indicated that defect clustering and ordering may both be valid diffusional pathways in the decomposition of alloys.[38]

The additional epitaxial phase sharing the (1 0 1) reflection of the rutile in Fig. 8 could be tentatively attributed to a nonstoichiometric low-symmetry phase with oxygen deficiency for specific crystallographic shear (CS) analogous to the case of nonstoichiometric TiO_{2-x}.[25,26] In this regard, the CS slip plane are $\{1\,\bar{2}\,1\}$ of the parent rutile structure for $TiO_{1.75} \sim TiO_{1.9}$,[25] and $\{1\,\bar{3}\,2\}$ for $TiO_{1.9} \sim TiO_{2.0}$.[26] The observed diffractions of the nonstoichiometric phase in Fig. 8 are in accord with the low-symmetry structures of these phases. However, the exact space group, composition and CS scheme of this phase is not clear. It is also beyond the scope of the present study to determine whether the same metastable precipitates are formed outside the other side (i.e. TiO_2-rich sample, as for 2T8S rather than 8T2S) of the spinodal.

4.4. Phase equilibrium and reorientation during reactive sintering

Phase equilibrium compositions were readily approached by reactive sintering the TiO_2 and SnO_2 powders rather than by decomposition of the solid solution as indicated by the XRD results of the samples fired at 1000 °C. Apparently, interdiffusion through short circuit path of the grain surface and grain boundaries would facilitate the solute redistribution during the process of reactive sintering.

Reactive sintering also caused reorientation of the embedded particles in the polycrystals. In fact, the size-dependent orientation change of the relatively small-sized SnO_2 particles in the TiO_2-rich rutile grain (Fig. 10) can be rationalized by a Brownian-type rotation of the particles in terms of anchorage release (i.e. debonding) at the SnO_2/TiO_2 interface analogous to the high-temperature dynamics of Y-PSZ particles in $Co_{1-x}O$

grains.[11] The diffusion coefficient (D) of spherical particles confined in a grain was formulated to decrease exponentially with the increase of number of atoms in anchorage (i.e. atoms in good coherency) at the interface, whereas increase exponentially with ΔT above a critical temperature (T_0) for anchorage release:[11]

$$D = 2a^2 \left(\frac{kT}{h}\right) \exp\left(\frac{\Delta S_0}{R}\right) \exp\left(\frac{-\Delta H_0}{RT}\right) \times \exp\left(\frac{-\pi d^2 \Delta h_m}{a^2 R}\right) \left(\frac{1}{T} - \frac{1}{T_0}\right) \quad (1)$$

where $\pi d^2/a^2$ is the number of atoms in anchorage (assuming crystallite as a sphere of diameter d), a the periodic distance of an atom, ΔG_0 ($= \Delta H_0 - T\Delta S_0$) for viscous motion in terms of atom diffusion along the interface, Δh_m the latent enthalpy to untie an atom from the interface, h the Planck constant and other symbols have their usual meanings.

T_0 and the free energy are in fact a function of the particle size due to the capillarity effect. Thus, the reasons that a smaller particle has a higher diffusivity are two-fold: firstly, a smaller number of atoms in anchorage at the interface; secondly, a lower T_0. The critical temperature T_0 for anchorage release at the SnO_2/TiO_2 rutile interface should be lower than 1000 °C in order to activate the Brownian motion of the embedded particles in the solid state at a moderate homologous temperature of 0.60–0.67 as mentioned. The smaller-sized and relatively SnO_2-rich particles would become even smaller upon reactive sintering, because of a considerable evaporation event of SnO_2,[28] and/or the SnO_2–TiO_2 interdiffusion, to facilitate Brownian rotation of the particles until energetically favored parallel epitaxial state was reached.

A considerable amount of vacancies due to interdiffusion of atoms across the interface is expected to benefit the anchorage release at the interface, hence facilitates particle rotation for the SnO_2/TiO_2 composite. This vacancy effect on debonding of atoms at interface can be further enhanced when there is considerable net vacancies flux to form Kirkendall pores. The strain as a result of interdiffusion may also cause a considerable softening, and thereby facilitate de-bonding of the composition variant phases formed by a reactive sintering process.

5. Conclusions

(1) Defect clusters and commensurate superstructures were formed in the TiO_2–SnO_2 solid solution of the rutile-type structure when quenched from 1600 °C in air.
(2) Spontaneous spinodal decomposition of the equimolar alloy of TiO_2–SnO_2 at 1000 °C caused composition fluctuation along the ***c***-axis with a semi-coherent (0 0 1) interface.
(3) The decomposition of the non-equimolar alloy outside the spinodal at 1000 °C caused metastable precipitation of an ilmenite-type and another epitaxial phase tentatively indexed as a nonstoichiometric phase.
(4) Reactive sintering at 1000 °C facilitated not only phase equilibrium but also the Brownian rotation of the small-sized SnO_2 particles until parallel epitaxial relationship with the TiO_2-rich host was reached.

Acknowledgements

Supported by the Center for Nanoscience and Nanotechnology of NSYSU and National Science Council, Taiwan.

Appendix A. Brownian motion of crystallites under 1 D, 2 D and 3 D constraints

In previous annealing studies of cubic oxide composites prepared by solid-state sintering, e.g. $Ni_{1-x}O$/yttria partially stabilized zirconia (Y-PSZ),[9] $Ni_{1-x}O/NiAl_2O_4$,[10] and $Co_{1-x}O$/Y-PSZ,[11] we have proved that intragranular particles can change orientation until they reach epitaxial relationships with respect to the host grains. A relatively high homologous temperature (T/T_m) for the $Ni_{1-x}O/NiAl_2O_4$,[10] and $Co_{1-x}O$/Y-PSZ composites[11] resulted in a faster orientation change and more significant coalescence of the particles than the $Ni_{1-x}O$/Y-PSZ composite at a specified annealing temperature of 1600 °C.[9] Reorientation of the intragranular particles in these composites has little to do with sintering,[12] diffusion induced recrystallization[13] or dynamic recrystallization,[14] but can be reasonably explained by rotation of the particles above a critical temperature for anchorage release at the interface with respect to the host grain.[9–12]

In such a thermally activated rotation process of the intragranular particles, Brownian motion of the particles in terms of interfacial diffusion of atoms was suggested to happen[9–12] as for the case of fcc metal crystallites migrating and rotating on single crystal substrate, KCl(1 0 0) with or without steps.[15–20] The size and temperature dependence of diffusivity of the crystallites has been measured over KCl(1 0 0),[15] and found to be in accordance with Brownian-type motion of the crystallites in terms of interfacial diffusion of atoms from leading edge to trailing edge of the crystallites. Einstein's molecular theory of heat,[21] Eyring's transition-state model[22] and frictional force at a viscous interface were thus adopted to formulate the diffusivity equation of the crystallite over the single crystal substrate.[16–18] The size dependence of orientation change of intragranular particles was also verified by annealing experiments for the case of $Co_{1-x}O$ particles in Y-PSZ grain.[11]

Appendix B

SEM (SEI) of (a) 2T8S sample sintered/homogenized at 1600 °C for 4 h followed by air-quenching to room temperature and then thermal etching at 1500 °C for 10 min, (b) 8T2S sample reactively sintered at 1000 °C for 72 h followed by air-quenching to room temperature and then chemical etching by 30 mol% HCl (added with two drops of HF) for 1.5 h.

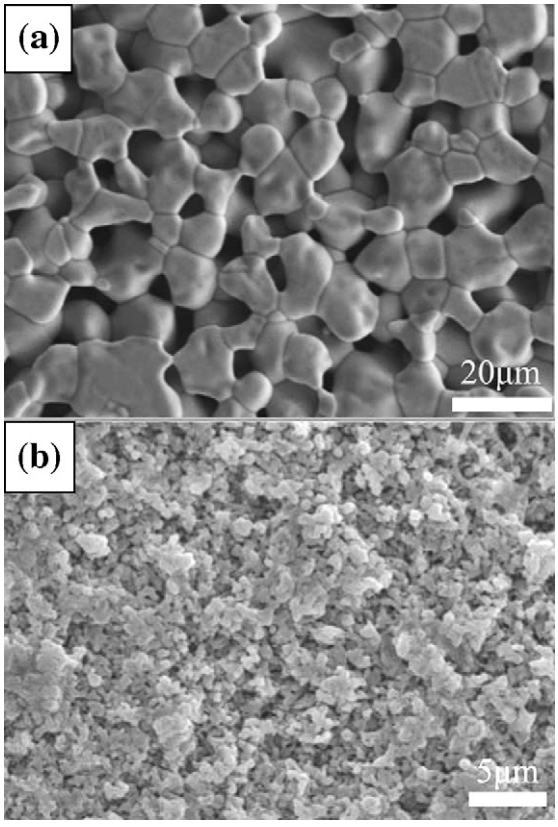

References

1. Padurow, N. N., Miscibility in the system rutile-cassiterite", Naturwissenschaften. *Naturwissenschaften*, 1956, **43**(17), 395–396.
2. Schultz, A. H. and Stubican, V. S., Modulated structures in the system TiO_2–SnO_2. *Phil Mag*, 1968, **18**, 929–937.
3. Stubican, V. S. and Schultz, A. H., Phase separation by spinodal decomosition in the tetragonal system. *J Am Ceram Soc*, 1970, **53**, 211–214.
4. Park, M., Mitchell, T. E. and Heuer, A. H., Subsolidus equilibria in the TiO_2–SnO_2 system. *J Am Ceram Soc*, 1975, **58**(1–2), 43–47.
5. Park, M., Mitchell, T. E. and Heuer, A. H., Decomposition of TiO_2–SnO_2 solid solutions. *J Mater Sci*, 1976, **11**, 1227–1238.
6. Yang, K. C. and Shen, P., On the precipitation of coherent spinel nanoparticles in Ti-doped MgO. *J Solid State Chem*, 2005, **178**, 661–670.
7. Yang, K. C., Shen, P. and Gan, D., Defect microstructures of TiO_2 rutile due to Zr^{4+} dissolution and expulsion. *J Solid State Chem*, 2006, **179**, 3478–3483.
8. Li, M. Y., Shen, P. and Hwang, S. L., Oxidation–decomposition facilitated reorientation of nanoparticles in reactively sintered $(Ni_{0.33}Co_{0.6})_{71-\delta}O$ polycrystals. *Mater Sci Eng A*, 2003, **343**, 227–234.
9. Chen, J. and Shen, P., On the rotation of nonepitaxial $Ni_{1-x}O$ particles within zirconia grain. *Scripta Mater*, 1997, **37**, 1287–1294.
10. Wang, S. R. and Shen, P., Rotation-coalescence of confined particles in $Ni_{1-x}O/NiAl_2O_4$ composites. *Mater Sci Eng A*, 1998, **251**, 106–112.
11. Lin, K. T. and Shen, P., Thermally activated rotation of $Co_{1-x}O$ particles within zirconia. *Mater Sci Eng A*, 1999, **270**, 125–132.
12. Rankin, J. and Sheldon, B. W., In situ TEM sintering of nano-sized ZrO_2 particles. *Mater Sci Eng A*, 1995, **204**, 48–53.
13. Doo, V. Y. and Balluffi, R. W., Structural changes in single crystal copper-alpha brass diffusion couple. *Acta Metall*, 1958, **6**, 428–438.
14. Poirier, J. P., *Creep of Crystals*. Cambridge University Press, Cambridge, 1985, pp. 260.
15. Masson, A., Métois, J. J. and et Kern, R., Migration brownienne de cristallites sur une surface et relation avec l'épitaxie I. Partie expérimentale. *Surf Sci*, 1971, **27**, 463–482.
16. Kern, R., Masson, A. and et Métois, J. J., Migration brownienne de cristallites sur une surface et relation avec l'épitaxie II. Partie théorique. *Surf Sci*, 1971, **27**, 483–498.
17. Métois, J. J., Gauch, M., Masson, A. and et Kern, R., Migration brownienne de cristallites sur une surface et relation avec l'épitaxie III cas de l'aluminium sur KCl: précisions sur le méchanisme de glissement. *Surf Sci*, 1972, **30**, 43–52.
18. Métois, J. J., Gauch, M., Masson, A. and et Kern, R., Épitaxie: phenomène de postnucleation sur L'exemple des couches minces discontinues d'aluminium et d'or sur (1 0 0) KCl. *Thin Solid Films*, 1972, **11**, 205–218.
19. Métois, J. J., Migration brownienne de cristallites sur une surface et relation avec l'épitaxie IV. Mobilité de cristallites sur une surface: décoration de gradins monoatomiques de surface. *Surf Sci*, 1973, **36**, 269–280.
20. Kuo, L. Y. and Shen, P., On the rotation of nonepitaxy crystallites on single crystal substrate. *Surf Sci*, 1997, **373**, L350–L356.
21. Einstein, A., In *Investigations on the Theory of the Brownian Movement*, ed. R. Fürth. Methuen, 1926, pp. 1–124 (Cowper, A.D., Trans.).
22. Gladstone, S., Laidler, K. and Eyring, H., *The Theory of Rate Processes*. McGraw-Hill, New York, 1941.
23. Shannon, R. D., Revised effective ionic radii and systematic studies of interatomic distances in halides and chalcogenides. *Acta Crystallogr A*, 1976, **32**, 751–767.
24. Banfield, J. F. and Veblen, D. R., The structure and origin of Fe-bearing platelets in metamorphic rutile. *Am Miner*, 1991, **76**, 113–127.
25. Andersson, S., The crystal structure of Ti_5O_9. *Acta Chem Scand*, 1960, **14**, 1161–1172.
26. Bursill, L. A. and Hyde, B. G., Crystal structure in the $\{1\bar{3}2\}$ family of higher titanium oxides Ti_nO_{2n-1}. *Acta Crystallogr B*, 1971, **27**, 210–215.
27. Cormack, A. N., Freeman, C. M., Catlow, C. R. A. and Royle, R. L., Defect structures and energetics in nonstoichiometric rutile. In *Advances in Ceramics, vol. 23. Nonstoichiometric Compounds*, ed. C. R. A. Catlow and W. C. Mackrodt. American Ceramic Soc., Westerville, OH, 1987, pp. 283–291.
28. Leite, E. R., Cerri, J. A., Longo, E., Varela, J. A. and Paskocima, C. A., Sintering of ultrafine undoped SnO_2 powder. *J Euro Ceram Soc*, 2001, **21**, 669–675.
29. Bueno, P. R., Leite, E. R., Bulhoes, L. O. S., Longo, E. and Paiva-Santos, C. O., Sintering and mass transport features of (Sn, Ti)O_2 polycrystalline ceramic. *J Eur Ceram Soc*, 2003, **23**, 887–896.
30. Kröger, F. A. and Vink, H. J., Relations between the concentrations of imperfections in crystalline solids. *Solid State Phys*, 1956, **3**, 307–435.
31. Khachaturyan, A. G., *Theory of Structural Transformations in Solids*. Wiley, New York, 1983, pp.342–49, 358–65.
32. Yuan, T. C. and Virkar, A. V., Kinetics of spinodal decomposition in the TiO_2–SnO_2 system: the effect of aliovalent dopants. *J Am Ceram Soc*, 1988, **71**(1), 12–21.
33. Wu, K. and Mendelson, K. S., Spinodal decomposition in the tetragonal system. *J Chem Phys*, 1973, **58**, 2929–2933.
34. Wittke, J. P., Diffusion of transition metal ions into rutile (TiO_2). *J Electrochem Soc*, 1966, **113**, 193–194.
35. Huntington, H. B. and Sullivan, G. A., Interstitial diffusion mechanism in rutile. *Phys Rev Lett*, 1965, **14**, 177–178.
36. Tsai, M. H., Chen, S. Y. and Shen, P., Imperfect oriented attachment: accretion and defect generation of nanosize rutile condensates. *Nano Lett*, 2004, **4**(7), 1179–1201.
37. Tseng, W. J., Shen, P. and Chen, S. Y., Defect generation of rutile-type SnO_2 nanocondensates: imperfect oriented attachment and phase transformation. *J. Solid State Chem*, 2006, **197**, 1230–1239.
38. Soffa, B., Diffusional pathways in the decomposition of alloys. In *Proceedings of the international conference on solid–solid phase transformation in inorganic materials*, 2005.